

Cosmic evolution of the star formation efficiency in Milky Way-like galaxies

Álvaro Segovia Otero^{1*}, Oscar Agertz¹, Florent Renaud^{1,2,3}, Katarina Kraljic², Alessandro B. Romeo⁴, and Vadim A. Semenov⁵

¹Lund Observatory, Division of Astrophysics, Department of Physics, Lund University, Box 43, SE-221 00 Lund, Sweden

²Observatoire Astronomique de Strasbourg, Université de Strasbourg, CNRS UMR 7550, F-67000 Strasbourg, France

³University of Strasbourg Institute for Advanced Study, 5 allée du Général Rouvillois, F-67083 Strasbourg, France

⁴Department of Space, Earth and Environment, Chalmers University of Technology, SE-41296 Gothenburg, Sweden

⁵Center for Astrophysics | Harvard & Smithsonian, 60 Garden St, Cambridge, MA 02138, USA

Accepted XXX. Received YYY; in original form ZZZ

ABSTRACT

Current star formation models are based on the local structure of the interstellar medium (ISM), yet the details on how the small-scale physics propagates up to global galactic-scale properties are still under debate. To investigate this we use VINTERGATAN, a high-resolution (20 pc) cosmological zoom-in simulation of a Milky Way-like galaxy. We study how the velocity dispersion and density structure of the ISM on 50-100 parsec scales evolve with redshift, and quantify their impact on the star formation efficiency per free-fall timescale, ϵ_{ff} . During epochs of starburst activity the star forming ISM can reach velocity dispersions as high as $\sim 50 \text{ km s}^{-1}$ for the densest and coldest gas, most noticeable during the last major merger event happening at $1.3 < z < 1.5$. After a phase dominated by mergers ($1 < z < 5$), VINTERGATAN transitions into a secularly evolving state where the cold neutral ISM typically features velocity dispersion levels of $\sim 10 \text{ km s}^{-1}$. Despite strongly evolving density and turbulence distributions over cosmic time, the local ϵ_{ff} at the resolution limit is found to change by only a factor of a few: from median efficiencies of 0.8% at $z > 1$ to 0.3% at $z < 1$. The corresponding mass-weighted average shows a universal $\langle \epsilon_{\text{ff}} \rangle \approx 1\%$, originating from an almost invariant distribution of virial parameters in star forming clouds, where changes in gas densities and turbulence levels are coupled such that the kinetic-to-gravitational energy ratio remains close to constant. Finally, we show that a *theoretically* motivated instantaneous efficiency such as ϵ_{ff} is intrinsically different to its *observational* estimates adopting tracers of star formation e.g. $\text{H}\alpha$. As signatures of the physical conditions that trigger star formation can be lost on short ($\sim 10 \text{ Myr}$) timescales, we argue that caution must be taken when constraining star formation models from observational estimates of ϵ_{ff} .

Key words: galaxies:star formation – ISM:structure – methods:numerical

1 INTRODUCTION

Current star formation theories strive to connect, and track across cosmic time, the local properties of star-forming regions ($\lesssim 100 \text{ pc}$), the global parameters characterising galaxies ($> \text{tens of kpc}$), and their cosmological environment. Nearby star-forming spiral galaxies follow the canonical main sequence (MS) and Kennicutt-Schmidt (KS) relations: at a given stellar mass, disc galaxies with larger molecular gas surface densities present greater star formation rate (SFR) surface densities, depleting their gas reservoirs on timescales of $\sim \text{few Gyr}$ (gas depletion times are estimated as $\tau_{\text{dep}} = M_{\text{gas}}/\text{SFR}$, Kennicutt 1998; Bolatto et al. 2008; Leroy et al. 2013; Speagle et al. 2014). The absence of major mergers combined with low gas fractions ($f_{\text{g}} \lesssim 10\%$ for $M_{\star} \gtrsim 10^{10} M_{\odot}$, e.g. Scholte et al. 2024) allow these isolated systems to develop stable rotationally-supported thin discs (Brinchmann et al. 2004; Wuyts et al. 2011; Wisnioski et al. 2015), where star formation on galactic scales is regulated by gas accretion, disc dynamics and instabilities, and feedback processes.

In the Local Universe, it is mainly within giant molecular clouds (GMCs) that the ISM is shielded from background radiation, reaching the required density and temperature conditions to trigger star formation (for a review, see McKee & Ostriker 2007). CO observations of GMCs in the Milky Way have revealed cloud scaling relations that relate their masses, sizes and velocity dispersions (Larson 1981; Solomon et al. 1987; Heyer et al. 2009; Miville-Deschênes et al. 2017). These have typical molecular gas surface densities of $\Sigma_{\text{gas}} \approx 100 M_{\odot} \text{ pc}^{-2}$, effective radii of $R \sim 10 - 100 \text{ pc}$, and velocity dispersions of $\sigma_{\text{gas}} \sim 1 - 10 \text{ km s}^{-1}$. These properties translate into cloud virial parameters of $\alpha_{\text{vir}} \approx 1 - 10$ (Leroy et al. 2016; Miville-Deschênes et al. 2017; Sun et al. 2022), where α_{vir} is defined as the ratio between the kinetic to gravitational energy such that $\alpha_{\text{vir}} = 2E_{\text{kin}}/|E_{\text{grav}}|$. A constant α_{vir} of $\gtrsim 1$ is often understood as GMCs reaching dynamical equilibrium, although external cloud confinement by thermal and turbulent pressure complicates this picture (e.g. Elmegreen 1989; Grisdale et al. 2018). Star formation under these conditions is inefficient, which is commonly quantified using the star formation efficiency per free-fall time parameter ϵ_{ff} , i.e. the fraction of stars formed from the total gas mass of a GMC on a free-

* alvaro.segovia@astro.lu.se

fall timescale $t_{\text{ff}} = \sqrt{3\pi/32G\rho}$. Observations of star-forming GMCs show ϵ_{ff} distributions with a universal average of 1%, followed by a spread of several orders of magnitude (see review by [Krumholz et al. 2019](#)). Preliminary systematic changes in ϵ_{ff} and α_{vir} have been found as a function of galactic environment (bulge, bars, spiral arms, disc), but the scatter around these parameters is dominated by intrinsic cloud-to-cloud differences ([Sun et al. 2020a,b](#); [Rosolowsky et al. 2021](#)). The way in which gas densities and velocity dispersions in the ISM are affected by environmental factors, and whether this has a significant impact on the local star formation properties, still remains unclear even at low redshift.

At high redshifts ($z > 1$), star-forming galaxies are predominantly rotating discs, and their high gas fractions make them gravitationally unstable to clump formation (for reviews see [Förster Schreiber & Wuyts 2020](#); [Saintonge & Catinella 2022](#)). Such a clumpy ISM is subject to strong feedback from enhanced SFRs, along with more frequent galactic interactions ([Duncan et al. 2019](#)). All of this sets elevated velocity dispersions at high redshifts, as measured from kinematics of molecular, atomic, and ionised gas tracers ([Übler et al. 2019](#), and references therein). Compared to spiral disc galaxies at present day, average gas depletion times in high- z galaxies are found to be shorter ($\tau_{\text{dep}} \geq 500$ Myr, see [Tacconi et al. 2018, 2020](#)). In contrast to low redshift discs, the global τ_{dep} in starburst galaxies is around an order of magnitude shorter (30-300 Myr, [Daddi et al. 2010](#); [Rodighiero et al. 2011](#)), making them a natural testbed for star formation physics in more extreme ISM conditions. Starbursts can be driven by mergers, but can also be triggered by secular processes in isolated gas-rich turbulent discs ([Ciesla et al. 2023](#)).

The star-forming gas clumps in starbursts observed to date are denser and more turbulent than GMCs in Local spirals, nevertheless, they also show $\alpha_{\text{vir}} \approx 1 - 10$, albeit with a large scatter ([Leroy et al. 2015](#); [Rosolowsky et al. 2021](#); [Dessauges-Zavadsky et al. 2023](#), see also [Krahn et al. 2024](#) for GMCs in the overlap region between the Antennae galaxies). Unfortunately, observations of gas clumps in such objects are scarce and limited to bright mergers in the Local Universe or lensed high-redshift galaxies ([Dessauges-Zavadsky et al. 2019](#)). It is therefore uncertain whether ISM conditions at high redshift or in extreme environments such as starbursts imply efficient local star formation, i.e. a higher ϵ_{ff} .

Mapping the density and turbulent structure of the ISM to its star formation properties has been the goal of theoretical and computationally-driven studies in the last couple of decades. Pioneering analytical work base the star formation process on the theory of supersonic isothermal gas ([Krumholz & McKee 2005](#); [Padoan & Nordlund 2011](#); [Hennebelle & Chabrier 2011](#); [Federrath & Klessen 2012](#); [Burkhart 2018](#)). These models, further calibrated on controlled magnetohydrodynamic (MHD) simulations of GMCs (5-500 pc in size, [Grudić et al. 2018, 2019](#)) and highly resolved ISM boxes (\sim few pc in length, [Federrath et al. 2010](#); [Federrath & Klessen 2013](#); [Federrath 2015](#)), can predict the commonly observed average $\langle\epsilon_{\text{ff}}\rangle \approx 1\%$ even though they locally present large ϵ_{ff} variations ([Krumholz et al. 2012](#)). More realistic set-ups face the challenge of resolving the large dynamic range that connects the inner structure of GMCs and their galactic and extra-galactic environment in isolated disc or cosmological simulations respectively. To that aim, sub-grid star formation recipes are either based on the aforementioned analytical prescriptions where ϵ_{ff} directly depends on the local gas density and velocity dispersion ([Semenov et al. 2016](#); [Trebitsch et al. 2017](#); [Kretschmer & Teyssier 2020](#); [Nuñez-Castiñeira et al. 2021](#)), or have a fixed ϵ_{ff} typically in the range of 1-100 percent ([Renaud et al. 2013](#); [Hopkins et al. 2018](#); [Grisdale et al. 2018, 2019](#)). These simulations reveal a complex interplay among the extra-galactic and galactic environ-

ment, star formation models, and stellar feedback prescriptions (e.g. [Agertz et al. 2011](#); [Agertz & Kravtsov 2015](#); [Semenov et al. 2018](#)). For this reason, different star formation models can yield significant differences in ISM and GMC properties (e.g. [Grisdale et al. 2017, 2018](#)), but be degenerate in terms of integrated quantities on galactic scales such as SFRs or global gas depletion times ([Hopkins et al. 2013a](#)).

In this paper we use VINTERGATAN ([Agertz et al. 2021](#); [Renaud et al. 2021a,b](#)), a cosmological zoom-in simulation of a Milky Way-like galaxy to investigate the evolution of the ISM and local star formation properties, i.e. ϵ_{ff} as a function of redshift. In our simulation, the [Padoan et al. \(2012\)](#) effective model connects the density and velocity dispersion of the ISM with ϵ_{ff} , which we further compare to Local Universe GMC observations from the PHANGS collaboration ([Schinnerer & Leroy 2024](#)). This work is a follow up of [Segovia Otero et al. \(2022\)](#) and [Renaud et al. \(2022\)](#), where we demonstrated the crucial role played by galaxy mergers and morphological transformations in setting the global gas depletion time. Here we focus on investigating the physics on smaller ($\lesssim 50 - 100$ parsec) scales and how it connects to the global properties of a galaxy across cosmic time. Section 2 briefly summarizes the simulation set-up, Section 3 highlights the connection between the cosmological environment and the local star formation properties of Milky-Way like galaxies, and Section 4 and 5 conclude with the main takeaways of this work and contextualise them with respect to other available models for star formation.

2 METHODOLOGY

The VINTERGATAN cosmological zoom-in simulation was run using the hydrodynamics+ N -body code RAMSES ([Teyssier 2002](#)), assuming Λ -cold dark matter (Λ CDM) cosmological parameters¹. The initial conditions correspond to the 'm12i' halo of the AGORA project ([Kim et al. 2014](#), [Kim et al. 2016](#), [Roca-Fàbrega et al. 2021](#), see also [Wetzel et al. 2023](#)), generated with the MUSIC code ([Hahn & Abel 2011](#)). Within a periodic box of 85 Mpc and 512^3 dark matter particles, the progenitor Lagrangian region is selected to be $3R_{200,m}$ around the halo at $z = 0$, where the virial radius and mass with respect to the mean cosmic background density at $z = 0$ are $R_{200,m} = 334$ kpc and $M_{200,m} = 1.3 \times 10^{12} M_{\odot}$ respectively. Its resolution was further enhanced to reach a dark-matter particle resolution of $3.5 \times 10^4 M_{\odot}$, and a mass and spatial resolution of $7070 M_{\odot}$ and $\lesssim 20$ pc respectively for the gas. A more exhaustive explanation of the technical aspects of the simulation can be found in [Agertz et al. \(2021\)](#). Here, we briefly emphasise on the relevant models applied to describe the galaxy formation physics within VINTERGATAN.

Star formation is treated as a Poisson process on a cell-by-cell basis (see [Agertz et al. 2013](#)), where the star formation rate density $\dot{\rho}_{\star}$ follows

$$\dot{\rho}_{\star} = \epsilon_{\text{ff}} \frac{\rho_{\text{g}}}{t_{\text{ff}}}, \quad \text{with } \rho_{\text{g}} > 100 \text{ cm}^{-3}, \quad \text{and } T_{\text{g}} < 100 \text{ K}. \quad (1)$$

Here, t_{ff} is the free-fall timescale and ϵ_{ff} is the star formation efficiency per free-fall time from [Padoan et al. \(2012\)](#) (henceforth, PN12). Star particles with an initial mass of $10^4 M_{\odot}$ form when gas is colder and denser than the density and temperature thresholds. These conditions are set to prevent thermally-supported gas from

¹ $H_0 = 70.2 \text{ km s}^{-1} \text{ Mpc}^{-1}$, $\Omega_{\text{m}} = 0.272$, $\Omega_{\Lambda} = 0.728$, $\Omega_{\text{b}} = 0.045$

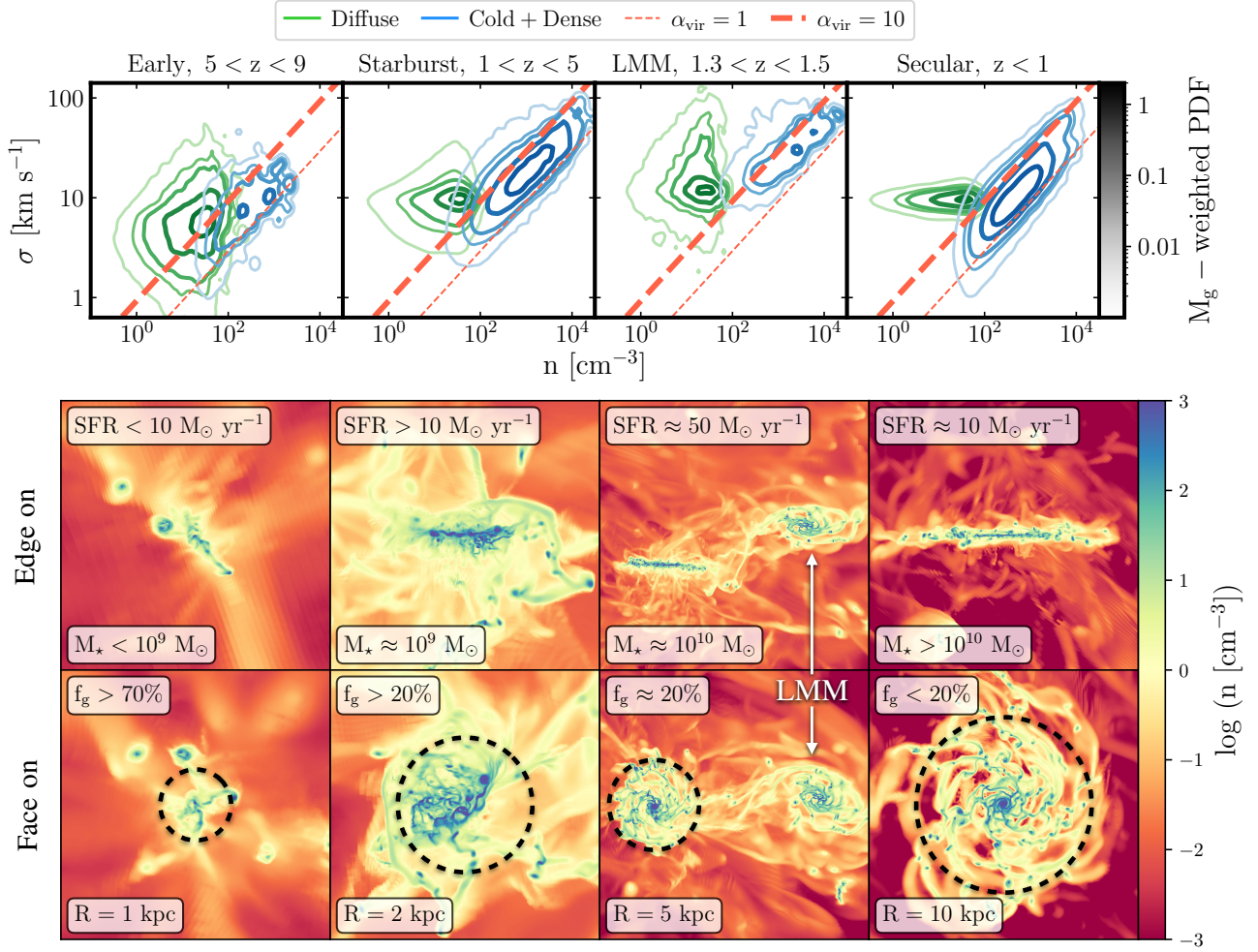


Figure 1. *Top:* Response of the ISM in VINTERGATAN as a function of redshift to its extra-galactic environment. For every redshift interval, each panel shows the distribution of the density n and velocity dispersion σ calculated from gas in $(50 \text{ pc})^3$ cubes. Contours represent the mass-weighted 2D histogram with probability densities of 0.6, 0.3, 0.1, 0.05, and 0.01 from thickest and darkest to thinnest and brightest contours respectively. Two sets of contours are presented: *cold+dense* (blue) for gas $T < 100 \text{ K}$ and $n > 100 \text{ cm}^{-3}$ (star-forming gas according to Equation 2); *diffuse* (green) for gas $T < 10^4 \text{ K}$ (excluding *cold+dense* gas). Dashed red lines of constant α_{vir} are included (Equation 3), computed on 50 pc scales for $\alpha_{\text{vir}} = 1$ (thin) and $\alpha_{\text{vir}} = 10$ (thick). *Bottom:* Snapshots of the evolution of VINTERGATAN. Each column represents the edge- and face-on views of the galaxy, colour-coded by its gas density at every cosmic epoch: *Early* ($5 < z < 9$), *Starburst* ($1 < z < 5$) including the *LMM* event from the first pericenter passage ($z \approx 1.5$) to the final coalescence of the merger ($z \approx 1.3$), and *Secular* ($z < 1$). Included in each panel is the SFR, computed from the mass of stars younger than 100 Myr, the total stellar mass M_\star , the gas fraction f_g , and twice the half radius calculated accounting for the spatial distribution of stars younger than 100 Myr (and outlined in black dashed circles on the bottom row panels). **Takeaway:** Density and velocity dispersion go hand in hand, specially for cold and dense gas, and respond to the cosmological environment: mergers stir the ISM towards high σ and n , when a more isolated disc has more lower turbulent levels and density values.

forming stars, a choice that has a minor impact on the overall star formation history as the free-fall timescales associated to such diffuse gas are long and do not contribute to the global SFR.

In PN12 they simulate star formation in supersonically turbulent, magnetized gas with a wide range of initial conditions and find that the star formation efficiency per free-fall time is well approximated by

$$\epsilon_{\text{ff}} = \epsilon_w \exp(-1.38\sqrt{\alpha_{\text{vir}}}) = \epsilon_w \exp\left(-1.6\frac{t_{\text{ff}}}{t_{\text{turb}}}\right). \quad (2)$$

The normalisation constant ϵ_w , here set to 0.5, accounts for processes such as mass loss via proto-stellar jets. The virial parameter is defined as

$$\alpha_{\text{vir}} = \frac{2E_{\text{kin}}}{|E_{\text{grav}}|} = \frac{15\sigma_{1D}^2}{\pi G \rho_g L^2} = 1.35 \left(\frac{t_{\text{ff}}}{t_{\text{turb}}}\right)^2, \quad (3)$$

where

$$t_{\text{turb}} = \frac{L}{2\sqrt{3}\sigma_{1D}} \quad (4)$$

is commonly referred to as the turbulence crossing time, which is on the order of the timescale for turbulent energy dissipation in the case of driven supersonic turbulence (Mac Low et al. 1998; Stone et al. 1998; Mac Low 1999). L is chosen to be the cell size ($\lesssim 20 \text{ pc}$), and σ_{1D} is the one-dimensional velocity dispersion calculated as the standard deviation of each component of the velocity vector independently for all 6 adjacent cells, i.e. effectively computed on $\sim 50 \text{ pc}$ scales, $\sigma_{1D}^2 = (\sigma_x^2 + \sigma_y^2 + \sigma_z^2)/3$.

The star formation model in PN12 is exclusively virial parameter-dependent. Alternatives exist, e.g. with additional Mach number dependencies (for a comprehensive discussion see [Federrath & Klessen 2012](#)), but have not been directly implemented in this work. In Section 4 we comment on the potential implications of using different prescriptions for ϵ_{ff} . It is also worth mentioning that even though sophisticated, these star formation laws do not directly account for the galactic scale environment surrounding the star-forming region, hence not accounting for mechanisms such as shear and large-scale compression.

Each star particle represents a single stellar population with a universal initial mass function (IMF, [Chabrier 2003](#)) and age-, mass-, and gas/stellar metallicity-dependent feedback processes such as radiation pressure, stellar winds, core collapse, and type Ia supernovae calibrated on the STARBURST99 code ([Raiteri et al. 1996](#); [Leitherer et al. 1999](#); [Kim & Ostriker 2015](#)). Gas metallicity is initialised from a floor of $Z = 10^{-3} Z_{\odot}$ in the zoomed-in region² and subsequently enriched with iron (Fe) and oxygen (O) by supernovae, where we adopt the yields from ([Woosley & Heger 2007](#)). This allows for metallicity-dependent cooling for $T < 10^4$ K ([Rosen & Bregman 1995](#)) and $10^4 < T < 10^{8.5}$ K gas ([Sutherland & Dopita 1993](#)). Gas heating from a UV radiation background was added assuming reionisation starting at $z = 8.5$ ([Haardt & Madau 1996](#); [Courty & Alimi 2004](#); [Aubert & Teyssier 2010](#)).

To extract reliable information from our data, we use robust statistics ([Müller 2000](#); [Romeo et al. 2023](#)). Namely, the median and median absolute deviation (MAD) provide reliable information on the 'central value' and 'width' of the sample even when a large fraction of them are outliers. The robust 1σ scatter is derived as $\text{MAD}/0.6745$. We further emphasize that using the median rather than the mean is convenient under logarithmic transformations given that $\text{med}[\log(X)] = \log[\text{med}(X)]$. The robust scatter in logarithmic scale is approximated to $\sigma_{\log(X)} \approx \sigma_X/[X \ln(10)]$, which is more representative in the limit where $\sigma_X/X \ll 1$.

3 RESULTS

VINTERGATAN proposes a formation channel general to nearby star-forming spirals that reproduces Milky Way features at $z \approx 0$ ([Agertz et al. 2021](#); [Renaud et al. 2021a,b](#)). [Segovia Otero et al. \(2022\)](#) demonstrate that Milky Way-like galaxies experience epochs of starburst or more quiescent star formation activity depending on the global gas depletion time of the cold ISM. They identify three evolutionary stages with order of magnitude changes in τ_{dep} : an *early* stage at high redshift ($5 < z < 9$) with $\tau_{\text{dep}} \sim 1$ Gyr; a *starburst* phase ($1 < z < 5$) when τ_{dep} drops by an order of magnitude driven by mergers impacting on an assembled galactic disc; a *secular* stage ($z < 1$) when τ_{dep} increases to a few Gyr in the absence of mergers. In the following, we explore how the density and turbulent structure of the ISM evolve with time depending on these epochs, and assess how much this affects the local star formation properties in the galaxy. Note that the word *local* is used in this work to refer to ISM properties derived on GMC scales when speaking about observations and for parameters computed on scales comparable to the size of gas cells in simulations. Conversely, the word *global* refers to galactic scales.

3.1 ISM density and velocity dispersion across cosmic time

Figure 1 shows the ISM in the aforementioned evolutionary stages of VINTERGATAN. An additional panel representing the last major merger (LMM) exemplifies the properties of the ISM from its first pericenter passage ($z \approx 1.5$) to its final coalescence with the main galaxy ($z \approx 1.3$). Maps showing the gas density of the main galaxy (face- and edge-on), its environment, and its main global properties at each phase are on the bottom. In the top panels, contours show the density and velocity dispersion levels of the ISM, computed by stacking simulation snapshots with an output resolution of 100 Myr within each redshift interval. The dashed red lines mark regions of constant virial parameters of $\alpha_{\text{vir}} = 1$ (thin) and $\alpha_{\text{vir}} = 10$ (thick) using Equation 3.

For every output, we select a spherical volume with radius equal to three times the stellar half-mass radius of the galaxy³ and split it in cubes of 50 pc in size. Within each cube we divide the gas into two phases by applying density and temperature cuts:

- The *cold+dense* ISM (blue contours) corresponds to gas that fulfills the star formation criteria from Equation 1, i.e. above $n > 100 \text{ cm}^{-3}$ and below $T < 100$ K. This phase traces molecular species ([Klessen & Glover 2016](#)). Densities are computed by dividing the corresponding mass of *cold+dense* gas by the volume of the 50 pc cube, and σ represents the one-dimensional mass-weighted standard deviation of the velocities in 50 pc cubes with more than one *cold+dense* gas cell.
- The *diffuse* ISM (green contours) includes all gas cells at temperatures of $T < 10^4$ K, excluding those with *cold+dense* gas properties. These density and temperature ranges are typical of the warm neutral or ionised medium traced by neutral hydrogen (HI) and recombination lines such as H α . Its densities and velocity dispersions have been computed in the same way as for the *cold+dense* gas, minding the new temperature and density cuts.

The velocity dispersion and density distributions for both *diffuse* and *cold+dense* gas phases evolve with cosmic epoch. This evolution happens at a constant virial parameter (see Section 3.2), with $\alpha_{\text{vir}} \geq 10$ for *diffuse* gas and at $1 < \alpha_{\text{vir}} < 10$ for *cold+dense* gas. In fact, *cold+dense* gas shows a positive correlation between the velocity dispersion and density with $\sigma \propto n^{0.5}$, in agreement with previous studies of disc galaxies ([Semenov et al. 2016](#)). Such a scaling is compatible with the Larson scaling relations ([Larson 1981](#); [Grisdale et al. 2018](#)) when a *fixed spatial scale* is considered. *Diffuse* gas has less inertia and is easier to accelerate, making it more susceptible to stellar feedback ([Ejdetjärn et al. 2022](#)) and the extra-galactic environment. Thus, it deviates from the $\sigma - n$ relation, with substantially more scatter, specially at $z > 1$.

During the *early* stage ($5 < z < 9$), most of the gas is found at velocity dispersion values of $\sigma \leq 30 \text{ km s}^{-1}$, which is in line with CII observations of galaxies in the $10^8 \leq M_{\star} \leq 10^{10} M_{\odot}$ mass range at these redshifts (left panel in Figure 1, see also [Pope et al. 2023](#); [Posses et al. 2023](#)). Although gas-rich and immersed in a merger-dominated environment, SFRs in VINTERGATAN are the lowest in its star formation history ([Segovia Otero et al. 2022](#), for observations of gas fractions see [Heintz et al. 2022](#); [Aravena et al. 2023](#), and [Fudamoto et al. 2022](#); [Leethochawalit et al. 2023](#); [Trussler et al. 2023](#) for SFRs of coeval systems). It is not until the galaxy enters the *starburst* stage ($1 < z < 5$) that the highest velocity dispersion levels are reached,

² This metallicity floor accounts for unresolved population III stars ([Wise et al. 2012](#); [Agertz et al. 2020](#)).

³ Galactic centers in each output are found by running a shrinking sphere algorithm, and half-mass radii are calculated from the mass of stars younger than 100 Myr within the virial radius of VINTERGATAN at each epoch.

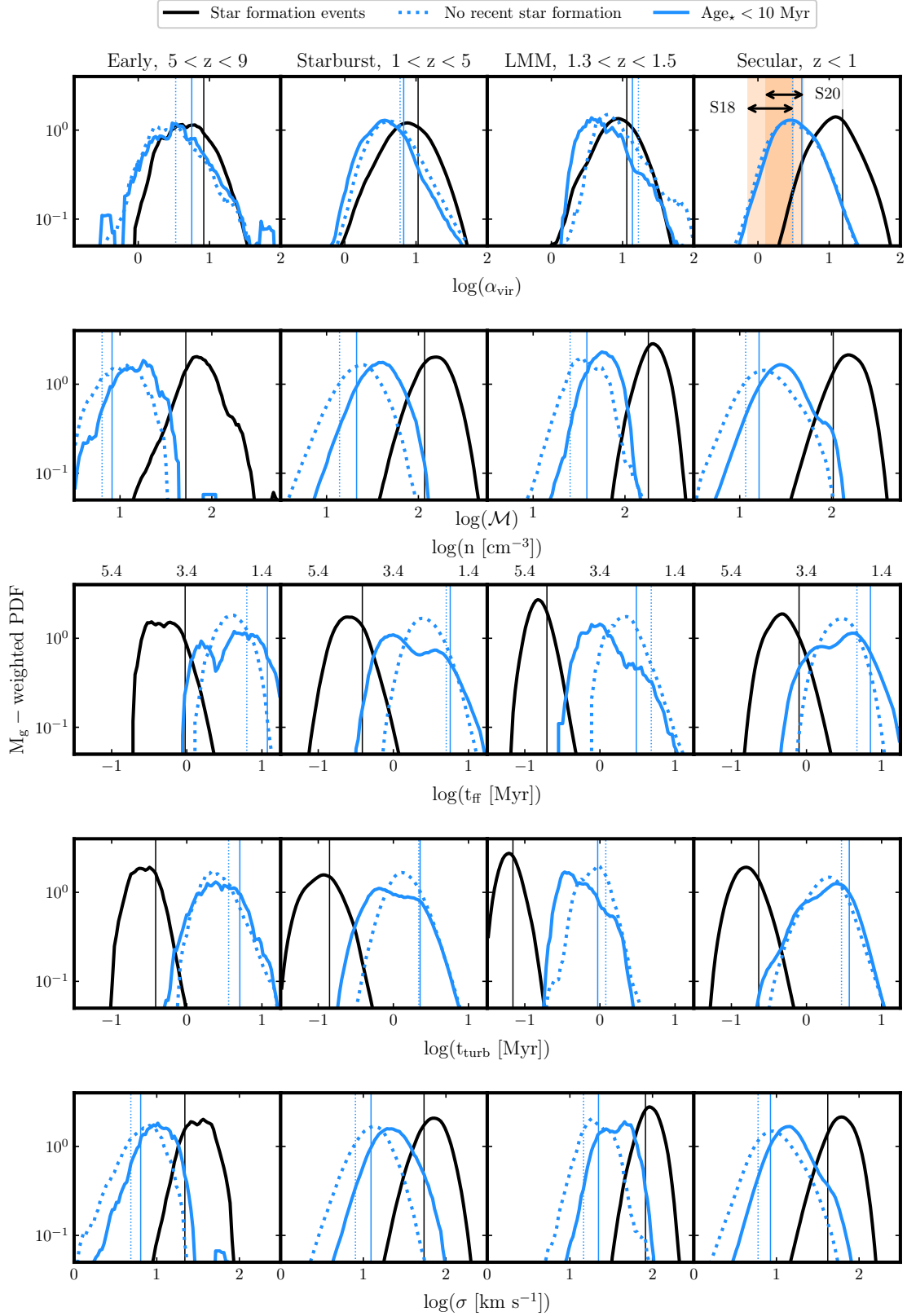


Figure 2. Gas mass-weighted PDFs of α_{vir} , \mathcal{M} , t_{ff} , the turbulent timescale t_{turb} , and velocity dispersion at each cosmic epoch in VINTERGATAN. PDFs plotted in solid black correspond to *SF-events* while those in blue represent *cold+dense* gas. Curves in solid blue show ISM properties evaluated on 50 pc cubes with star particles younger than 10 Myr. Those in dotted blue PDFs characterise the ISM with no recent star formation. Additionally, vertical lines correspond to the median values of each distribution with same colour and line style. The orange rectangles in the top right panel represent the scatter (robust standard deviation, see last paragraph in Section 2) in α_{vir} values evaluated on 80 pc in Sun et al. (2018) and 90 pc in Sun et al. (2020b). Black arrows are just included to clarify the extent of the scatter. **Takeaway:** Even if the density and turbulence of the ISM on 50 pc scales changes with cosmic epoch, the virial parameter shows a roughly constant distribution as a function of redshift.

especially in the case of the *LMM* event for both gas phases (central panels in Figure 1). This is in agreement with observed starbursting discs slightly more massive than VINTERGATAN at similar redshifts ($\sigma \approx 20 - 80 \text{ km s}^{-1}$ also from CII measurements, [Herrera-Camus et al. 2022](#); [Roman-Oliveira et al. 2023](#); [Parlanti et al. 2023](#); [Rizzo et al. 2023](#)). With the assembly of a galactic disc at $z \approx 4.8$, mergers tidally compress gas, triggering star formation on short depletion times due to an excess of gas in the *cold+dense* phase ([Segovia Otero et al. 2022](#); [Renaud et al. 2022](#)). Nevertheless, even if an excess of gas at high densities leads to high SFRs (which inevitably goes hand-in-hand with increased stellar feedback), disentangling the roles of feedback- and gravity/compression-driven turbulence is challenging in cosmological zoom-in simulations (but see [Renaud et al. 2014](#), who tell both effects apart using high time-resolution simulations of idealised mergers). In the absence of major mergers (*secular* stage, $z \lesssim 1$), and with the depletion of gas reservoirs, SFRs and velocity dispersion values decrease most notably in the *diffuse* gas ($\sigma < 10 \text{ km s}^{-1}$ for HI observations in Local spirals, [Tamburro et al. 2009](#); [Eibensteiner et al. 2023](#)). Consequently, its scatter also decreases substantially.

3.2 Properties of the cold and dense ISM

Densities reached in VINTERGATAN imply free-fall timescales at least a factor of ten shorter than the output frequency of the simulation ($\sim 100 \text{ Myr}$). Thus, to get insight into the actual ISM properties upon star formation we use the *star formation events* (hereafter *SF-events*) gas. This data-set is different to the previous two gas phases in that they have not been extracted directly from the low-cadence outputs of the simulation. *SF-events* properties are logged on the fly from gas cells that have undergone star formation: densities are directly read from the star-forming cell ($\lesssim 20 \text{ pc}$), and velocity dispersion values are calculated using the velocity vectors of the six adjacent cells ($\sim 50 \text{ pc}$). *SF-events* gas is represented in solid black in Figure 2, revealing very turbulent ($\geq 50 \text{ km s}^{-1}$), dense ($\geq 10^4 \text{ cm}^{-3}$), and cold ($\approx 10 \text{ K}$) properties that resemble those that make molecules such as HCN, HCO^+ , NH_3 , CH, CN, and CS ([Klessen & Glover 2016](#); [Gallagher et al. 2018b](#); [Wilson et al. 2023](#)).

From this point on we focus our analysis on the *cold+dense* and *SF-events* gas in order to connect the ISM structure with its star formation properties at each cosmic epoch. Figure 2 shows the evolution of α_{vir} (Equation 3), Mach number⁴, t_{ff} , t_{turb} (Equation 4), density, and velocity dispersion for *SF-events* gas in black and *cold+dense* gas in blue. *Cold+dense* gas is further split in two: gas within 50 pc cubes containing stars younger than 10 Myr in solid blue; gas cubes without star particles younger than 10 Myr in dotted blue. It is worth noting that the velocity dispersion values in both *cold+dense* and *SF-events* gas are computed at approximately the same scales, but other properties such as t_{ff} (or c_s) are derived from the density (or mass-weighted average temperature) on 50 pc cubes compared to reading off the star-forming cell properties on $\lesssim 20 \text{ pc}$ before spawning a star particle. We emphasize that our goal here is to: *i*) analyse the properties of the ISM at the resolution limit of the simulation where the PN12 star formation model actually comes

into play; *ii*) compare the distributions of *SF-events* and *cold+dense* properties; *iii*) compare VINTERGATAN to GMC scaling relations from the PHANGS collaboration, who provide GMC properties on a variety of scales (45-150 pc, [Rosolowsky et al. 2021](#); [Sun et al. 2023](#); [Schinnerer & Leroy 2024](#)).

The most striking result in Figure 2 is the difference between the *SF-events* and the *cold+dense* gas distributions. Note that the distributions are normalised, so *SF-events* gas actually conforms a smaller sample of cells representing the more extreme regions of the $\sigma - n$ space. An order of magnitude shift to shorter t_{ff} and t_{turb} dynamical timescales is seen, highlighting the importance of capturing these short-lived events, and implying that *SF-events* gas is indeed a biased subset of denser and more turbulent gas intimately connected to stellar feedback. To explore this idea, we compare *cold+dense* gas with and without recent star formation (solid and dotted blue in Figure 2). We find that gas embedding stars younger than 10 Myr reach denser and more turbulent states, i.e. stronger resemblance to *SF-events* distributions. The same trends are recovered when defining recent star formation as stars younger than 5 Myr and 100 Myr (timescales probed by $\text{H}\alpha$ and UV observations respectively), with stronger shifts between recent and past star forming ISM the older the stellar age cut is.

Looking at the *cold+dense* distributions, the shortest t_{ff} and t_{turb} are achieved during the *LMM* event compared to the other epochs (third and fourth rows in Figure 2), expected from the evolution of the corresponding density and velocity dispersion distributions. Nevertheless, both dynamical timescales conspire to render an α_{vir} PDF that is roughly constant in all four cosmic epochs (top row in Figure 2), with median values of $\alpha_{\text{vir}} \approx 4.4$ and robust scatter of 3.3. Approximately stationary α_{vir} distributions with time is also noticed for *SF-events* gas, which overlap substantially with *cold+dense* gas ones despite the stark differences between them. This is particularly the case at $z > 1$, with both *SF-events* and *cold+dense* α_{vir} distributions showing marginally larger median values. In merger-driven environments at these redshifts, higher α_{vir} values are observed in recent simulations by [He et al. \(2023\)](#), yet CO observations of GMCs in mergers and lensed turbulent discs at $z > 1$ cannot conclusively estimate a systematic change. Some studies point towards $\alpha_{\text{vir}} \approx 1$ in both mergers and isolated galaxies ([Dessauges-Zavadsky et al. 2019, 2023](#)), whereas others report increased α_{vir} values in starbursts, low density regions, galactic center environments, and even mergers ([Leroy et al. 2015](#)). For the particular case of the Antennae galaxies, the order of magnitude increase in physical resolution to $\sim 10 \text{ pc}$ from [Krahm et al. \(2024\)](#) compared to [Wei et al. \(2012\)](#) renders an average of $\langle \alpha_{\text{vir}} \rangle = 13.80 \pm 7.84$.

In the absence of mergers during the *secular* phase, the median α_{vir} is around a factor of three larger in *SF-events* gas with respect to *cold+dense*. Such moderate shift to lower virial parameters in *cold+dense* gas is due to lower velocity dispersion values increasing t_{turb} , and is in good agreement with CO-based observations of GMCs in nearby galaxies⁵ (highlighted in orange boxes on the top right panel in Figure 2, [Sun et al. 2018, 2020b](#); [Rosolowsky et al. 2021](#)). On the other hand, *SF-events* experiences an increase in α_{vir} due to the fact that less gas is compressed to dense states, creating longer

⁴ The expression for the Mach number is $\mathcal{M} = \sqrt{3}\sigma_{\text{ID}}/c_s$, where c_s is the thermal sound speed determined by the temperature of gas in the cell T , the Boltzmann constant k_B , a mean molecular weight of $\mu = 1.3$, and the mass of hydrogen m_H so that $c_s = \sqrt{k_B T / \mu m_H}$. Note that the sound speed for both *cold+dense* and *SF-events* gas is $c_s \lesssim 1 \text{ km s}^{-1}$, making turbulence supersonic for all measured values of the velocity dispersion.

⁵ Our equation for α_{vir} is almost identical to that of [Sun et al. \(2018\)](#) and [Sun et al. \(2020b\)](#), except that in their work they use the projected gas surface density, $\Sigma_g = \pi R^2$, where R is the depth of the line of sight. They also add a geometrical factor f that corrects for an assumed radial density profile of CO inside their spherical GMCs so that $f = (1 - \gamma/3)(1 - 2\gamma/5)$, where γ is the slope of the power-law of the profile ([Bertoldi & McKee 1992](#); [Rosolowsky & Leroy 2006](#)).

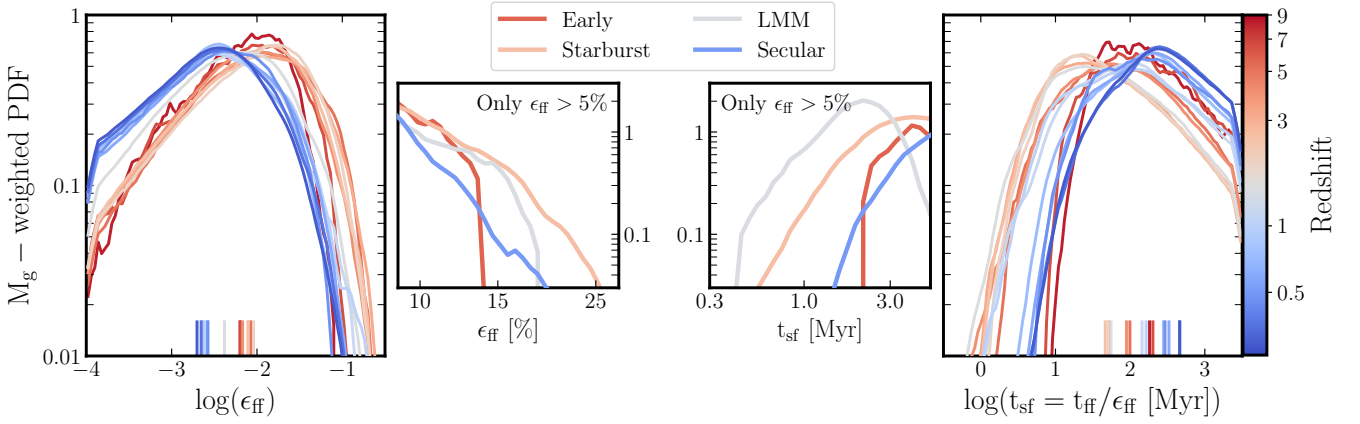


Figure 3. Cosmic evolution of the ϵ_{ff} gas mass-weighted PDFs (left) and local star formation timescales (right) in 15 redshift bins. The on-the-fly ϵ_{ff} is calculated with Equation 2 (Padoan et al. 2012), using *SF-events* properties as input. Small line markers at the bottom the left and rightmost panels indicate the evolution of the median ϵ_{ff} and t_{sf} respectively. Two additional panels display the re-calculated PDFs for only cells with $\epsilon_{\text{ff}} > 5\%$ (center left). For clarity, 4 colour-coded PDFs show the averaged distributions for each cosmic epoch. **Takeaway:** $\langle \epsilon_{\text{ff}} \rangle \approx 1\%$ is constant throughout cosmic time, and therefore the local timescales for star formation are mostly dependent on the changes in the gas density PDFs, through t_{ff} .

t_{ff} on average. As we mentioned previously, if we take *SF-events* to resemble dense gas tracers, its α_{vir} values overestimate the HCN-based virial parameters (Gallagher et al. 2018a; Jiménez-Donaire et al. 2019; Neumann et al. 2023), which agree better with CO-based observations.

Additionally, we have checked that our results are robust to small changes to the spatial scale by repeating the analysis using 100 pc cubes, with no change to the main conclusions drawn here.

3.3 Implications for the local ϵ_{ff}

We next turn to the resulting ϵ_{ff} distributions for the *SF-events* gas. The leftmost panel in Figure 3 presents the evolution of the ϵ_{ff} and local depletion time PDFs with redshift. Given that the PN12 model is α_{vir} -dependent, a weakly increasing virial parameter with time (solid black in Figure 2) leads to a weak decrease of ϵ_{ff} . The mass-weighted mean of ϵ_{ff} is approximately 1%, in agreement with the universally observed and predicted values (Krumholz et al. 2012; Lee et al. 2016; Utomo et al. 2018; Semenov et al. 2016; Grisdale et al. 2019; Semenov et al. in prep., see also Polzin et al. 2024 where $\langle \epsilon_{\text{ff}} \rangle \approx 1\%$ for a range of metallicities). We can rewrite the local star formation law in Equation 1 as $\rho_{\text{g}}/\dot{\rho}_{\star} = t_{\text{ff}}/\epsilon_{\text{ff}}$, where $t_{\text{sf}} = t_{\text{ff}}/\epsilon_{\text{ff}}$ is the local gas depletion time. Then, in our case where the gas upon star formation in our simulation features a nearly constant ϵ_{ff} , $t_{\text{sf}} \propto t_{\text{ff}}$. This means that changes to the local rate of star formation are mainly driven by changes in the density PDF (as $t_{\text{ff}} \propto \rho_{\text{g}}^{-0.5}$). The rightmost panel of Figure 3 shows the evolution of t_{sf} . During the *starburst* and *LMM* epochs, both t_{sf} and t_{ff} (third row of Figure 2) shifts to shorter timescales, which is coeval with the drop of global depletion time values seen in Segovia Otero et al. (2022), caused by tidal compression and shocks during galaxy interactions (Renaud et al. 2022). In this picture, the role of increased levels of ISM turbulence is therefore *not* to impact the distribution of ϵ_{ff} on small scales, but rather to drive the ISM density PDF towards higher densities, which in turn leads to lower global gas depletion times (see also Kraljic et al. 2014, 2024). We note that the median t_{sf} is an order of magnitude shorter (~ 100 Myr) than the global depletion time τ_{dep} (~ 1 Gyr) due to the fact that most gas is not star forming (Semenov et al. 2017; Polzin et al. 2024).

The shape of the distributions, along with the median values (markers on the bottom of Figure 3), reveal a slight evolution with time: red distributions showing symbolically higher ϵ_{ff} medians at $z > 1$ (0.8%) and a family of blue distributions with a factor of ~ 3 lower ϵ_{ff} after the *LMM* event (0.3%). Given the span of the ϵ_{ff} PDFs (0.001%–30%) and the more drastic evolution of t_{ff} and t_{turb} , we consider ϵ_{ff} to be roughly stationary. However, this change in efficiency is enough for parts of the ISM in the *starburst* and *LMM* periods to feature ϵ_{ff} above $\sim 20\%$. These star-forming regions contain the largest amount of dense turbulent gas, but as can be seen from the PDFs, they make out a small fraction of the total gas mass of the galaxy during that epoch ($\geq 2\%$ during the *starburst* phase compared to $< 0.5\%$ for the *secular* and *early* epochs). They also correspond to the shortest timescales (< 1 Myr), potentially making them ideal locations for massive star cluster formation (Li et al. 2018, 2020, 2022).

In Section 4 we discuss how alternatives to PN12 could affect our conclusions.

3.4 Inferring ϵ_{ff} from observations

A large number of studies have been undertaken to constrain ϵ_{ff} using Milky Way GMC- and cloud-scale observations of Local Universe galaxies (for reviews, see Krumholz et al. 2019; Schinnerer & Leroy 2024) as well as in gravitationally lensed high- z galaxies (e.g. Dessauges-Zavadsky et al. 2019, 2023). An apples-to-apples comparison with theory and simulations is not trivial (see Grudić et al. 2018, 2019, for high resolution GMC simulations, Grisdale et al. 2019 for simulations of isolated disc galaxies, Nuñez-Castiñeira et al. 2021 for cosmological simulations, and Bemis & Wilson 2023 for a more observational perspective). Observationally, ϵ_{ff} quantifies the ratio between recent star formation and total mass budget of GMCs, normalised by t_{ff} , and probed by molecular gas and SFR tracers. Therefore, a time-lag exists between the actual trigger of star formation in a specific cloud, and the eventual signal of recent star formation (YSOs or H α , where the latter has an associated time-lag on the order of ~ 10 Myr). In contrast, in the context of theories of star formation in gravo-turbulent isothermal gas, ϵ_{ff} measures the amount of gas mass that is turned into stars on a free-fall timescale by integrating a log-normal density PDF above a certain density threshold. Such an

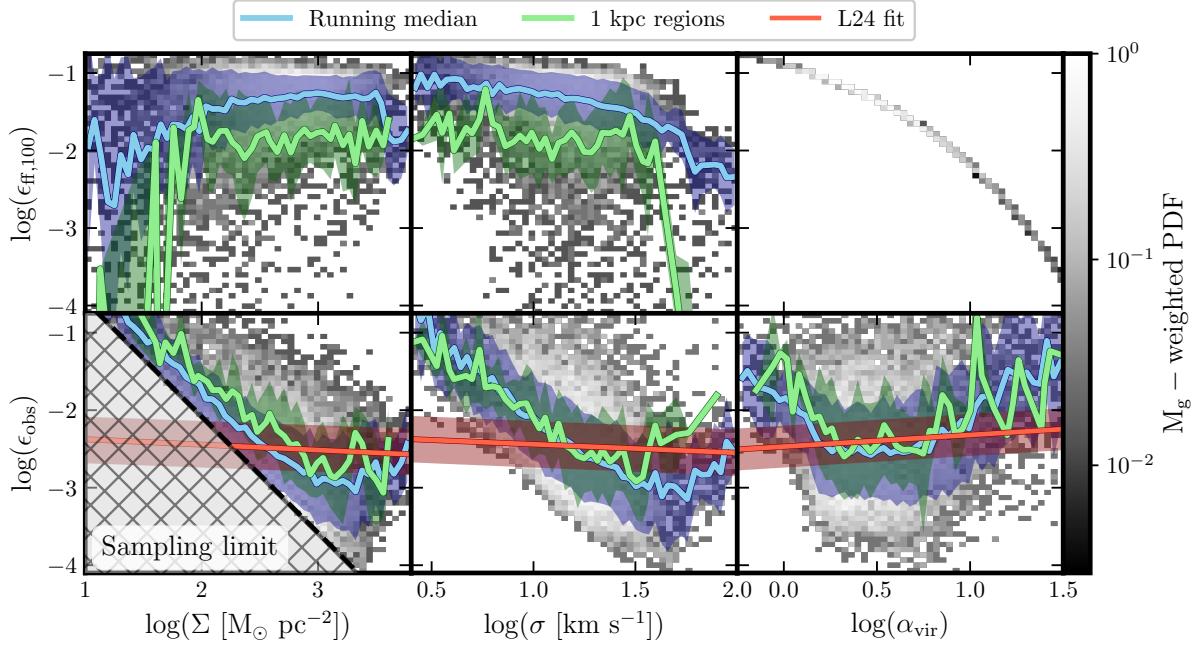


Figure 4. Theoretical (*top row*) and observational (*bottom row*) estimates of the star formation efficiencies per free-fall time as a function of Σ , σ and α_{vir} . Only *cold+dense* gas properties in outputs at $z < 1$ are used. The running median of the 2D histograms analysed on a grid of cubes of 100 pc in size is shown in blue, with its robust standard deviation as blue shaded band (see Section 3.2). In solid green we have the PHANGS-like running median also with its associated robust standard deviation band evaluated over on a grid of 1 kpc cubes (see Section 3.4 for a more thorough explanation on how to calculate PHANGS-like properties). In addition, the bottom row contains the empirical fit from Leroy et al. (2024) in prep. (L24), as well as the region where VINTERGATAN is limited by the mass resolution of star particles when sampling the star formation model. **Takeaway:** Star formation models based on the theory of isothermal gravo-turbulent gas relaxes the apparent contradiction seen between models of star formation and star formation scaling relations observed in GMCs.

instantaneous description of ϵ_{ff} is derived from the current density and turbulent structure of a piece of the ISM. This is not necessarily equal to an ϵ_{ff} inferred from gas tracers which encodes star formation imprinted at an earlier instance of a gas cloud.

In Figure 4 we use VINTERGATAN outputs in the *secular* phase of evolution ($z < 1$) to compute theoretically- and observationally-motivated estimates of ϵ_{ff} . The top row shows 2D histograms with their running medians and robust standard deviations in blue corresponding to the *theoretical* star formation efficiency per free-fall time, $\epsilon_{\text{ff},100}$, against the gas surface density, velocity dispersion, and virial parameter of *cold+dense* gas. This time, we calculate $\epsilon_{\text{ff},100}$ on a grid of 100 pc-sized cubes using Equation 2 from the velocity dispersion on these scales, and the density from the mass of *cold+dense* gas within each 100 parsec cube. Note that these measurements are not necessarily the same as the on-the-fly data in Figure 3 due to the larger sizes of the cubes with respect to the maximally resolved cells, and the inclusion of more diffuse and less turbulent gas (Figure 3). We shift our analysis from 50 parsec to 100 parsec because we want to compare the predictions of the PN12 model applied on 100 pc scales with the observational ϵ_{ff} estimates provided by the PHANGS collaboration, most of which are also on physical sizes of ~ 100 parsecs (Rosolowsky et al. 2021; Sun et al. 2022). The analysis behind Figure 4 was also performed on 50 pc scales, but no major differences were observed.

The bottom row in Figure 4 row shows a similar analysis, only applying an *observational* estimator for the star formation efficiency per free-fall time (Leroy et al. 2017; Schinnerer & Leroy 2024), hereafter ϵ_{obs} :

$$\epsilon_{\text{obs}} = \frac{t_{\text{ff}}}{\tau_{\text{dep}}}. \quad (5)$$

Here, t_{ff} and τ_{dep} are the local free-fall and gas depletion timescales computed from the *cold+dense* gas embedding stars younger than 10 Myr. Alternatives to Equation 5 have been put forward by, e.g. Lee et al. (2016)⁶, but our findings and main trends are not affected by the change of ϵ_{obs} prescription.

It is clear from Figure 4 that $\epsilon_{\text{ff},100}$ and ϵ_{obs} are dramatically different measurements. Starting with the $\epsilon_{\text{ff}}-\Sigma$ relations, $\epsilon_{\text{ff},100}$ increases with increasing Σ , as expected from a decreasing α_{vir} with increasing local density. The opposite trend is found for ϵ_{obs} , which stems from dense gas often probing early stages of GMCs, when only low levels of star formation have occurred and before feedback has had time to disrupt them. This yields a low mass ratio between young stars and the total mass of clouds, hence a low ϵ_{obs} . The high- ϵ_{obs} , low- Σ regions of the distribution tend to represent gas-poor clouds in their final stages of evolution, where large amounts of young stars drive large estimates of ϵ_{obs} (Feldmann & Gnedin 2011; Grudić et al. 2018, 2019; Grisdale et al. 2019). In contrast, such diffuse environment makes the instantaneous $\epsilon_{\text{ff},100}$ predict very low star formation efficiencies. We note however, that the picture is much more complex than this; for instance, as seen from the $\epsilon_{\text{obs}}-\alpha_{\text{vir}}$ relation, regions with apparent high ϵ_{obs} are in fact found to be both the most bound ($\alpha_{\text{vir}} < 1$) as well as unbound ($\alpha_{\text{vir}} > 10$), which indicates that not all

⁶ $\epsilon_{\text{obs}} = \frac{t_{\text{ff}}}{t_{y,\star}} \frac{M_{y,\star}}{M_{\text{g}} + M_{y,\star}}$, with $M_{y,\star}$ being the mass of stars younger than $t_{y,\star}$.

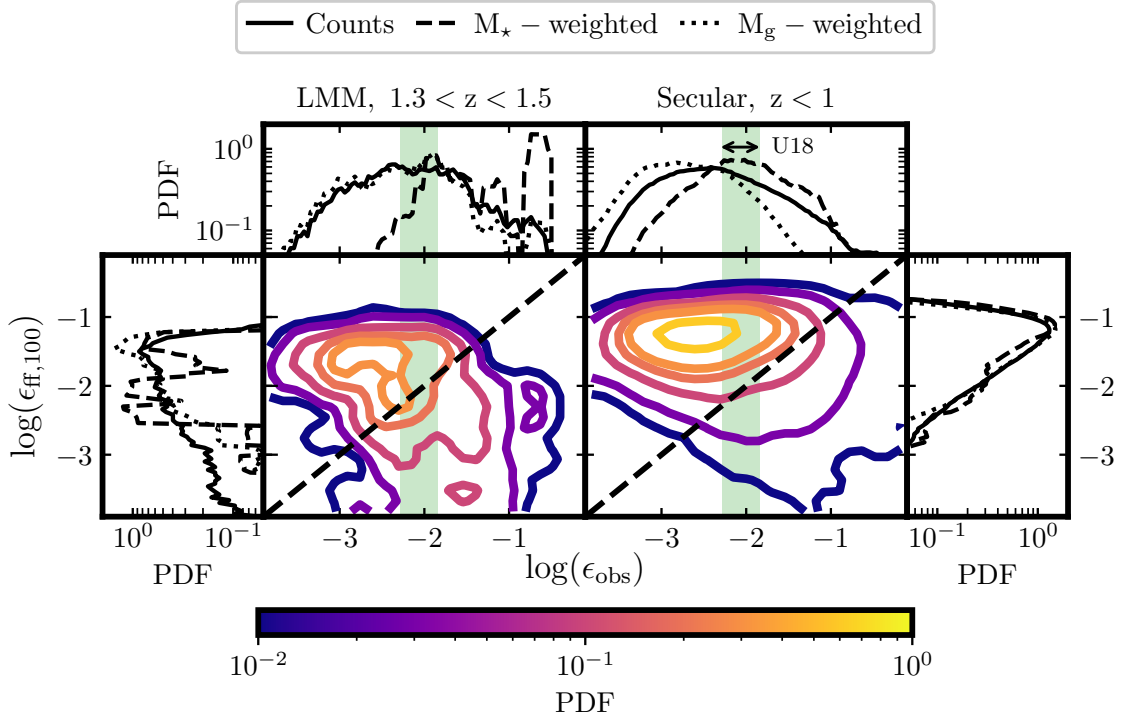


Figure 5. Comparison between the *theoretically-* (Padoan et al. 2012) versus the *observationally-* motivated efficiency (Equation 5) for the *LMM* and the *secular* phases of VINTERGATAN. Both quantities are evaluated on 100 pc scales, with colour-coded contours representing the 2D histogram between ϵ_{obs} and $\epsilon_{\text{ff},100}$ indicating probability densities of 0.6, 0.3, 0.2, 0.1, 0.03, 0.01 from most yellow to most purple respectively. The corresponding 1D histograms are placed on the top and sides of the main panels, where the solid curve representing the counts is weighted by stellar mass from particles younger than 10 Myr inside the 100 pc cubes (dashed) and by the enclosed gas mass (dotted). The diagonal dashed line crossing the two main panels just shows the one-to-one correlation between ϵ_{obs} and $\epsilon_{\text{ff},100}$. For comparison, the robust scatter of ϵ_{obs} from Utomo et al. (2018) is highlighted as a green rectangle. **Takeaway:** ϵ_{obs} and $\epsilon_{\text{ff},100}$ do not correlate with each other.

regions are necessarily undergoing late stages of star formation and feedback disruption (for an example of diverse cloud evolutionary paths, see figure 3 in Grisdale et al. 2019).

The $\epsilon_{\text{ff}}-\sigma$ relations predict a decreasing trend for both theoretical and observational efficiencies, yet additional efforts are required to precisely quantify whether such correlations are driven by the coupling between a multi-phase ISM and different stellar feedback mechanisms (see Discussion section, but also Federrath 2015; Andersson et al. 2024) or whether more large-scale sources of turbulence ought to be considered, e.g. shear⁷.

To ascertain whether the star formation properties in VINTERGATAN at low redshifts are compatible with observations, we compare our results to resolved (100 parsec scales) results from the PHANGS collaboration. The empirical fit from Leroy et al. (2024) in prep. (hereafter L24) with its 1σ scatter is included in orange for all bottom panels in Figure 4. This fit was performed using cloud properties measured on pixels of 50-150 pc in size further averaged over 0.5-1.5 kpc domains and weighted by the intensity of the CO (2-1) emission line (for more information see Sun et al. 2022, 2023; Schinnerer & Leroy 2024). To closely mimic such analysis, each of the VINTERGATAN outputs at $z < 1$ are now split in 1 kpc-sized regions. We then find which of the 100 pc cubes are located within

each kpc region and re-calculate the gas mass-weighted average over the kpc domain of Σ , σ , α_{vir} , and t_{ff} . It is worth emphasizing that we do not evaluate mass-weighted averages of cell values on kpc scales, but rather use those calculated from the 100 pc-sized cubes. ϵ_{obs} is still computed using Equation 5, but we now take the gas mass-weighted free-fall time, $\langle t_{\text{ff}} \rangle$, and divide it by the gas depletion times of each kpc domain.

Solid green lines in Figure 4 show the running median and associated scatter through these kpc domains. We see that VINTERGATAN and PHANGS agree well mostly at low ϵ_{obs} values, namely, in the high- Σ , high- σ regime of the parameter space. The most striking result is appreciated in the last column of Figure 4. While $\epsilon_{\text{ff},100}$ naturally follows the PN12 star formation law with an exponential shape, the ϵ_{obs} estimator recovers an almost constant star formation efficiency for virial parameters between $1 < \alpha_{\text{vir}} < 10$ in accordance with PHANGS analysis. While the match between ϵ_{obs} in VINTERGATAN and PHANGS is interesting, it remains to be seen if observed ϵ_{obs} trends can be used to constrain star formation models, or whether any signature of an underlying star formation law becomes washed out due to complex overlap of diverse cloud life cycles in a single ISM patch (see Grisdale et al. 2019). For instance, we note that the scatter in the simulation data is greater than that of the PHANGS fit. More analysis of simulations adopting a variety of star formation and feedback models is necessary to ascertain to what degree the scatter carries information of actual cloud diversity and ISM environment, as opposed to numerical aspects. Making use of outliers to cloud distribution (e.g. cloud mass) has the potential for providing more

⁷ Cold+dense gas in the *secular* phase of VINTERGATAN is often located within the inner half-mass radius of the galaxy, where galactic shear has been shown to play a crucial role in shaping the local star formation properties in the ISM of these regions ('the Brick', Petkova et al. 2023).

robust insights into the physics of star forming clouds (Renaud et al. 2024).

The match between VINTERGATAN and PHANGS at $\Sigma < 100 \text{ M}_\odot \text{ pc}^{-2}$ and $\sigma < 100 \text{ km s}^{-1}$ is poor. Part of the reason for this mismatch is inherent to VINTERGATAN and other cosmological simulations when sampling star formation using massive star particles, here with initial masses of 10^4 M_\odot . Such high masses cannot adequately sample low levels of star formation in low density gas, hence introducing a bias. To illustrate this we added a sampling limit⁸ with functional form $\epsilon_{\text{obs}} \propto 1/\Sigma^{1.5}$. This region of the parameter space is unreachable by our cosmological simulation and seen as a hatched grey region limited by a black dashed line in the bottom left panel of Figure 4. Higher resolution simulations are necessary to better probe star formation in the low density parts of the ISM, which we leave for future work.

4 DISCUSSION

In this paper we have studied how the density and velocity dispersion of the ISM in a Milky Way-mass galaxy evolve with cosmic time. Gravity and turbulence in gas clouds evolve conjointly, leading to an α_{vir} distribution that is almost constant in time. Applying the PN12 recipe for star formation, we get that the local theoretical efficiency is $\langle \epsilon_{\text{ff}} \rangle \approx 1\%$ computed on 20 pc scales. This is in good agreement with observational efficiency estimators, e.g. in the PHANGS collaboration. In the following section we discuss in depth how mapping between the theoretical and observational efficiencies would be affected by the life cycle of clouds, merger-driven environments at high redshift, and alternative implementations of star formation.

4.1 Mapping between theoretical and observational efficiencies

Figure 5 explores the mapping between ϵ_{obs} and $\epsilon_{\text{ff},100}$ over time by presenting $\epsilon_{\text{obs}}-\epsilon_{\text{ff},100}$ contours, and their corresponding 1D histograms for the *LMM* event (left hand side, $1.3 < z < 1.5$) and the *secular* epoch (right hand side, $z < 1$). The distributions of counts appear as solid curves, gas mass-weighted distributions are illustrated in dotted lines, and stellar mass-weighted ones in dashed lines. Both main panels suggest a tentative anti-correlation between ϵ_{obs} and $\epsilon_{\text{ff},100}$.

Right hand side panels in Figure 5 show the $\epsilon_{\text{obs}}-\epsilon_{\text{ff},100}$ relation for VINTERGATAN at $z < 1$. Surprisingly, an order of magnitude difference exists between a median $\epsilon_{\text{ff},100}$ of $\sim 4\%$ (rightmost panel) and a median ϵ_{obs} of $\sim 0.4\%$ (top right panel) regardless of the distributions being stellar or gas mass-weighted. This suggests that: *i*) from a PN12 point of view the ISM is considered to be more efficiently star-forming on 100 pc scales and free-fall timescales of $\sim 3.5 \text{ Myr}$ than what ϵ_{obs} implies; *ii*) the observational estimator ϵ_{obs} describes a less efficiently star forming ISM with gas depletion times of $\sim 300 \text{ Myr}$. From Figure 4 we concluded that star-forming clouds in their initial stages of evolution are dense and turbulent, with gas masses larger than that of stars younger than 10 Myr, appearing inefficient when traced by observations yet efficient as predicted by

theory. Contour lines in Figure 5 do show a tendency towards the low- $\epsilon_{\text{ff},100}$, high- ϵ_{obs} corner of the panel indicating such cloud evolution. Nevertheless, some of these early clouds are found in the central regions of VINTERGATAN and have the highest SFRs, so even after the onset of the first SNe, it is not clear whether feedback will be able to couple to such large cold and dense gas reservoirs to impact α_{vir} (Querejeta et al. 2019, see Hopkins et al. 2013b for feedback-regulated star formation, where SNe feedback weakly couples to cold and dense gas clouds with high HCN/CO compared to pre-SNe feedback, Ohlin et al. 2019 for tests of SNe explosions in turbulent ISM boxes, and Zakardjian et al. 2023 for spatial offsets between HCN and CO peaks).

During the *LMM* phase, VINTERGATAN is undergoing a starburst. Panels on the left hand side of Figure 5 illustrate how the $\epsilon_{\text{obs}}-\epsilon_{\text{ff},100}$ trend remains visible in a high- z major merger, almost orthogonal to the one-to-one relation (black dashed line). If we look at the distribution of counts or gas mass-weighted ϵ_{ff} values (solid and dotted respectively), there is a minor tendency towards lower $\epsilon_{\text{ff},100}$ and higher ϵ_{obs} compared to the *secular* phase, with median $\epsilon_{\text{ff},100} \sim \epsilon_{\text{obs}} \sim 1\%$ (leftmost and top left panels). In turn, the stellar mass-weighted ϵ_{obs} distributions are significantly shifted towards high efficiencies of $\sim 10\%$ (dashed lines). This is because shorter local gas depletion times of $\sim 100 \text{ Myr}$ (Figure 2), imply that there is an enhancement of star formation on shorter timescales when VINTERGATAN is observed as a starburst galaxy rather than a main-sequence galaxy. On 100 pc scales, this translates into larger stellar-to-gas mass ratios, which skews the stellar-mass weighted ϵ_{obs} distributions. Such efficiency values have been reported from YSOs in dense clumps in the Milky Way (Heyer et al. 2016), dense gas tracers like HCN and CS from extra-galactic sources (Wu et al. 2010), and from dense star forming regions in starbursting high-redshift lensed galaxies (Dessauges-Zavatsky et al. 2019, 2023).

Interestingly, the $\epsilon_{\text{ff},100}$ distribution indicates less efficient star formation during the *LMM* (leftmost panel) than in the *secular* phase (rightmost panel) due to enhanced α_{vir} . This is at odds with Figure 3, which characterises VINTERGATAN as a marginally less efficient galaxy after the *LMM* as gas is no longer in high density states. Even though both $\epsilon_{\text{ff},100}$ and ϵ_{ff} are computed using Equation 2, differences arise due to the different scales in which these parameters are computed, but most importantly due to the fact that *SF-events* and *cold+dense* describe inherently different states of gas. Namely, *SF-events* only include gas that has eventually formed a star, with moderately larger velocity dispersion values yet substantially denser gas. This makes up for an ϵ_{ff} evolution that follows changes in the gas density PDF.

Our results indicate that the multi-scale aspect of deriving star formation efficiencies as well as the use of different SFR and molecular gas tracers ought to be considered. These will weigh ϵ_{ff} distributions differently and imply various degrees of feedback coupling to the surrounding ISM that must ultimately be taken into account when comparing star formation models to observational estimators (Utomo et al. 2018; Krumholz et al. 2019; Schinnerer & Leroy 2024, and references therein).

4.2 Alternative star formation efficiency models

In this section we discuss how our findings could be affected when changing sub-grid recipes for star formation, and how can that modify the structure of the ISM. In order to illustrate the sensitivity of ϵ_{ff} to different star formation recipes, Figure 6 illustrates three ϵ_{ff} models for a fixed gas distribution, i.e. for the same cell density and velocity

⁸ The sampling limit is computed from Equation 5, re-writing it as $\epsilon_{\text{obs}} = t_{\text{ff}}/\tau_{\text{dep}} = (t_{\text{ff}}/t_{y,\star}) \cdot (\Sigma_{y,\star}/\Sigma)$. Re-formulating the free-fall time as $t_{\text{ff}} \propto (\Sigma/L)^{-0.5}$ we get that $\epsilon_{\text{obs}} \propto \sqrt{L}/t_{y,\star} \cdot \Sigma_{y,\star}/\Sigma^{1.5}$. Here, $\Sigma_{y,\star}$ corresponds to a maximally resolved star particle $\sim 10^4 \text{ M}_\odot$ inside a circle of radius equal to $L/2$ where $L = 100 \text{ pc}$, and $t_{y,\star}$ is the maximum age of young stars set to 10 Myr (Figure 2).

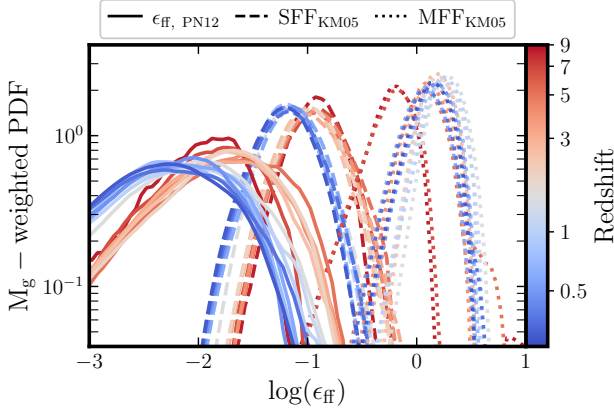


Figure 6. Comparison among three ϵ_{ff} models and the evolution of their gas mass-weighted PDFs with redshift. While the solid lines outline the on-the-fly ϵ_{ff} PDFs in VINTERGATAN, the same n and σ from the *SF-events* gas is used as input in the other two models. No additional simulations have been run with different ϵ_{ff} models. From left to right we have: ϵ_{ff} , PN12 solid lines represent the PN12 prescription, SFF_{KM05} dashed distributions stand for the single free-fall model adopted by Federrath & Klessen (2012) from Krumholz & McKee (2005), and the MFF_{KM05} in dotted PDFs correspond to the multi free-fall adaptation of the SFF_{KM05} based on Hennebelle & Chabrier (2011). **Takeaway:** The same on-the-fly density and velocity dispersion values are used as inputs for all models, so it is just a prove of concept that, *a priori*, different models result in different ϵ_{ff} distributions.

dispersion input without directly re-running VINTERGATAN for a self-consistent ISM:

- **PN12:** star formation prescription used in the VINTERGATAN simulation, presented in Equations 1 and 2 (solid lines in Figure 6). This model has been calibrated on high resolution simulations of magnetised ISM boxes (Padoan et al. 2012) that cover a range in virial parameters of $0.3 \geq \alpha_{\text{vir}} \geq 13$. The main take away from the PN12 model is that ϵ_{ff} exponentially decreases with increasing $t_{\text{ff}}/t_{\text{turb}}$, and changes by less than a factor of two with magnetic field strength for typical star forming regions.
- **SFF_{KM05} :** single free-fall models (SFF) define a family equations that explicitly integrate the log-normal distribution of gas densities to calculate the fraction of dense gas above a critical density that undergoes star formation on a *fixed* free-fall timescale⁹. Dashed curves in Figure 6 outline the star formation model based on equation 20 in Krumholz & McKee (2005), and further adapted by Federrath & Klessen (2012) (see their table 1). In this model, the free-fall time is fixed to that of the average density of the cloud.
- **MFF_{KM05} :** multi-free-fall models (MFF) as dotted curves in Figure 6 describe a family of star formation equation similar to SFF ones only that they allow the critical density threshold to vary given that

⁹ $\epsilon_{\text{ff}} = \frac{\epsilon_w}{\phi_t} \int_{s_{\text{crit}}}^{\infty} \frac{t_{\text{ff}}(\rho_0)}{t_{\text{ff}}(\rho)} \frac{\rho}{\rho_0} p(s) ds$, with $p(s)$ being the log-normal distribution of $s = \ln(\rho/\rho_0)$, s_{crit} the critical density equal to $(\pi^2/5)\phi_x^2 \times \alpha_{\text{vir}} M^2$ for the hydrodynamics-only case in both the SFF_{KM05} and MFF_{KM05} models (Federrath & Klessen 2012), and $t_{\text{ff}}(\rho)$ is the free-fall timescale set to $t_{\text{ff}}(\rho_0)$ in SFF_{KM05} but kept inside the integral for MFF_{KM05} . Both ϕ_t and ϕ_x are calibration factors set to $1/\phi_t = 3$ and $\phi_x = 0.12$ for SFF_{KM05} and $1/\phi_t = 0.49$ and $\phi_x = 0.19$ for MFF_{KM05} in Figure 6. The turbulent forcing parameter is $b_{\text{turb}} = 0.38$, representing a mix of solenoidal and compressive modes of turbulence

gravitationally bound structures of different densities will collapse at different t_{ff} (see Hennebelle & Chabrier 2011, and table 1 in Federrath & Klessen 2012).

The main takeaway from Figure 6 is that, the choice of ϵ_{ff} prescription shifts the emerging $\langle \epsilon_{\text{ff}} \rangle$. Both SFF_{KM05} and MFF_{KM05} render $\langle \epsilon_{\text{ff}} \rangle$ of 10% and 100% respectively. Nevertheless, we insist on the fact that a rigorous comparison would involve explicitly resolving the star formation-feedback cycle, leading to potentially different observables such as the KS relation, global τ_{dep} evolution across cosmic time, etc.

From the α_{vir} distributions in Figure 2 we see that at large fraction of the star-forming ISM has virial parameters that exceed those of the MHD ISM boxes used for the calibration of PN12, with Mach numbers approaching ~ 100 . These are extreme conditions, where PN12 is extrapolated beyond its α_{vir} limits towards values below 1 percent. Both SFF_{KM05} and MFF_{KM05} are α_{vir} and M dependent, meaning that for the same cell density input, additional dependencies on its velocity dispersion will shift ϵ_{ff} distributions towards more efficient values. That is particularly the case for the MFF_{KM05} model, with an extra factor $\exp[(3/8)\sigma_s^2]$, where $\sigma_s = \ln(1 + b^2 M^2)$. In the future we will evolve self-consistently these models using VINTERGATAN physics for strict comparison.

The role of turbulence is critical in regulating star formation (Re-naud et al. 2012; Kraljic et al. 2024), but the details in which it does so still remain unsettled. The reason is that since the dynamical range of the turbulent cascade of energy is not fully resolved in simulations, sub-grid recipes are developed to compensate for the effect of the small-scale turbulent eddies. In a recent study, Brucy et al. (2024a,b) emphasise that the density PDF at high Mach numbers can even depart from the often assumed log-normal PDF shapes (Castaing 1996; Hopkins 2013). These are promising simulations of high resolution isothermal ISM boxes that will soon be tested in the context of isolated disc and cosmological simulations. Semenov et al. (2016) implemented the sub-grid scale turbulent model (SGS, Schmidt & Federrath 2011; Schmidt et al. 2014) where the production and dissipation of unresolved turbulent energy is followed explicitly and used to calculate α_{vir} and ϵ_{ff} . Their isolated galaxy simulation well reproduces observed ϵ_{ff} distributions and the KS relation, but lacks the cosmological context. In fact, their work will be extended to cosmological zoom-in simulations in Semenov et al. in prep., where a near-universal ϵ_{ff} of $\sim 1\%$ is also found when modelling the local variations of ϵ_{ff} from the explicitly followed turbulent energy on unresolved scales. Kretschmer & Teyssier (2020) and Nuñez-Castiñeira et al. (2021) recently ran cosmological simulations using MFF in combination with SGS models and compare it to a constant ϵ_{ff} of 1 percent. They noticed how ϵ_{ff} is much more sensitive to the cosmological environment than what we see in VINTERGATAN. They conclude that it is the combination of star formation and feedback that regulates the structure of the ISM and eventually the emerging GMC and galactic-scale star formation scaling relations.

One of the main results from the FIRE collaboration (Faucher-Giguère et al. 2013; Hopkins et al. 2014; Orr et al. 2018; Hopkins et al. 2018; Feldmann et al. 2023) is that feedback is central to regulating star formation. At sufficiently high resolution, gas cools down, becomes increasingly dense, and forms stars until feedback disperses the cloud (see discussion in Hopkins et al. 2012). Hopkins et al. (2011) argue that a lower value of ϵ_{ff} simply allows for gravitational collapse to proceed for longer, eventually leading to a short enough $t_{\text{sf}} = t_{\text{ff}}/\epsilon_{\text{ff}}$, allowing for fast local star formation and clustered feedback, which in turn leads to cloud disruption. However, while changes to ϵ_{ff} , as well as the criteria for star formation, can lead

to little-to-no impact on integrated quantities on galactic scales, e.g. global SFRs, the emerging structure of the ISM can vary significantly (e.g. Hopkins et al. 2013a).

When feedback is not as efficient, it is ϵ_{ff} that regulates star formation (Semenov et al. 2017). The ϵ_{ff} can even lead to diverging global properties such as SFRs (Benincasa et al. 2016) or the normalisation of the KS relation (factor of a few, Agertz et al. 2013). We ultimately want to understand the underlying agent that determines how much gas mass and on which timescales does it pile up at the threshold of star formation. Targeting GMC properties like those in Figure 4 stand as stringent probes to distinguish star formation models, but as concluded from our results and along with previous studies, ϵ_{ff} alone does not fully inform on the SFR in the cell. It is the star formation-feedback cycle that eventually regulates star formation and that will set the observed ϵ_{ff} (see discussion in Federrath 2015).

5 CONCLUSIONS

In this paper we analyse the density and velocity dispersion of the ISM and its implications on the local star formation efficiency per free-fall time in VINTERGATAN, a high resolution cosmological zoom-in simulation of a Milky Way-type galaxy (Ageritz et al. 2021). We follow the evolution of their PDFs in the context of JWST observations (Heintz et al. 2022; Aravena et al. 2023), lensed galaxies and mergers around the cosmic peak of star formation (Dessauges-Zavadsky et al. 2019, 2023; Rizzo et al. 2023; Roman-Oliveira et al. 2023), and GMC observables at $z \approx 0$ from the PHANGS collaboration (Sun et al. 2018, 2020b; Rosolowsky et al. 2021; Schinnerer & Leroy 2024, Leroy et al. 2024 in prep.). Our findings can be summarised in four points:

- **The density and turbulent structure of the star forming ISM on 50 pc scales reacts to its extra-galactic environment** (Figure 1). Three cosmic epochs are identified: *i*) *early on* ($5 < z < 9$), where the gas-rich proto-galaxy is being assembled mostly from in-situ star formation and minor contributions from neighbouring galaxies that sustain moderate velocity dispersions levels ($\sigma < 30 \text{ km s}^{-1}$, Pope et al. 2023; Posses et al. 2023); *ii*) a *starburst* epoch ($1 < z < 5$) that ends with the *last major merger* event ($1.3 < z < 1.5$), where the galaxy builds a rotationally supported disc and experiences merger-driven starbursts that compress the ISM to $\sigma \approx 100 \text{ km s}^{-1}$ (Herrera-Camus et al. 2022; Parlanti et al. 2023) with global gas depletion times of $\sim 0.1 \text{ Gyr}$ due to an excess of gas at high densities; *iii*) a final *secular* phase where VINTERGATAN settles into an extended main sequence galaxy where $\sigma \approx 10 \text{ km s}^{-1}$ (Tamburro et al. 2009).
- **The density and velocity dispersion distributions on 50 pc scales evolve with cosmic time, but conspire to yield virial parameter distributions that are nearly constant** (Figure 2). The resulting ISM at low redshift has virial parameter distributions within $1 < \alpha_{\text{vir}} < 10$, values that are in agreement with observations (Leroy et al. 2015; Miville-Deschênes et al. 2017; Dessauges-Zavadsky et al. 2019; Rosolowsky et al. 2021). The more exposed the ISM is to recent star formation, and therefore affected by the subsequent stellar feedback, the denser and more turbulent it is. The presence of mergers, or absence thereof, pushes the ISM to such extreme conditions, nevertheless, their exact role in shaping α_{vir} distributions is still unclear.
- **The emerging ϵ_{ff} distribution spans several orders of magnitude, from 0.001% up to 30%, but averages to a roughly constant $\langle \epsilon_{\text{ff}} \rangle \approx 1\%$ across cosmic time** (Figure 3) in line with observations (Lee et al. 2016; Utomo et al. 2018; Krumholz et al. 2019) and recent computationally-driven studies (Semenov et al. 2016; Kretschmer &

Teyssier 2020; Nuñez-Castiñeyra et al. 2021; Polzin et al. 2024). The model adopted in VINTERGATAN is based on Padoan et al. (2012) and is exclusively α_{vir} -dependent. Thus, for a constant ϵ_{ff} the local gas depletion time scales as $t_{\text{sf}} \sim t_{\text{ff}}/\epsilon_{\text{ff}} \sim t_{\text{ff}} \propto \rho_{\text{g}}^{-0.5}$. As such, changes in the gas density PDFs become the main controlling factor in setting the local rate of star formation. The role of turbulence is to instead establish the density PDF in the first place (Kraljic et al. 2014; Renaud et al. 2014; Segovia Otero et al. 2022; Kraljic et al. 2024), rather than inducing large changes to ϵ_{ff} .

- **Theoretical, more instantaneous star formation efficiencies are inherently different to their observational estimators as they represent GMCs in different physical states** (Figure 4). Different star-forming gas tracers (CO, HCN, CS, etc.) probe a range of densities and temperatures. Tracers of recent star formation (YSOs, $\text{H}\alpha$, UV, etc.) also provide information about the star-forming cloud, but it must be *integrated* over the lifetime of the tracer employed (Grudić et al. 2019). This often hinders us from accessing the local instantaneous conditions for star formation. Figure 5 hints towards a possible anti-correlation between the theoretical and observational ϵ_{ff} , proposing that clouds in their initial stages of evolution begin with high $\epsilon_{\text{ff},100}$ and low ϵ_{obs} , and end their lives with low $\epsilon_{\text{ff},100}$ and high ϵ_{obs} . Our conclusions cast light onto seemingly contradictory results between star formation models and observations of star-forming GMC (Schruba et al. 2019). This behaviour is consistent with PHANGS observations (Leroy et al. 2017; Schinnerer & Leroy 2024, Leroy et al. 2024 in prep).

Linking local star formation parameters from ISM properties is highly non-linear and complex and has to rely on well calibrated sub-grid models (Nobels et al. 2024). These are rapidly improving with time (see Girma & Teyssier 2024, who include magnetic fields and Polzin et al. 2024 who add a metallicity dependency), but still do not consider the effects of the larger-scale environment (e.g. shear, compression, etc.).

In summary, star formation models, while degenerate, can be singled out when comparing to observed ISM properties. Moreover, information can be obtained from the scatter in GMC scaling relations, but how exactly it can help constrain star formation models is yet to be pinned down. In our work we stress the need for understanding the coupling among star formation, feedback, and a multi-phase ISM. Thus, a change in star formation models must go hand-in-hand with a change in the feedback recipe. Further observational data will be soon available in the advent of upcoming JWST and ALMA observations, and the further development of dedicated surveys like PHANGS and MANGA, generating multi-scale multi-wavelength data products of cloud properties.

ACKNOWLEDGEMENTS

We are deeply grateful to Adam K. Leroy for providing the empirical data from the PHANGS Collaboration and to Marta Reina Campos for insightful discussions. OA and ASO acknowledge support from the Knut and Alice Wallenberg Foundation, the Swedish Research Council (grant 2019-04659), and the Swedish National Space Agency (SNSA Dnr 2023-00164). FR acknowledges support provided by the University of Strasbourg Institute for Advanced Study (USIAS), within the French national program Investment for the Future (Excellence Initiative) IdEx-Unistra. Support for VS was provided by Harvard University through the Institute for Theory and Computation Fellowship.

DATA AVAILABILITY

The data underlying this article will be shared on reasonable request to the corresponding author.

REFERENCES

- Agertz O., Kravtsov A. V., 2015, *ApJ*, **804**, 18
- Agertz O., Teyssier R., Moore B., 2011, *MNRAS*, **410**, 1391
- Agertz O., Kravtsov A. V., Leitner S. N., Gnedin N. Y., 2013, *ApJ*, **770**, 25
- Agertz O., et al., 2020, *MNRAS*, **491**, 1656
- Agertz O., et al., 2021, *MNRAS*, **503**, 5826
- Andersson E. P., Mac Low M.-M., Agertz O., Renaud F., Li H., 2024, *A&A*, **681**, A28
- Aravena M., et al., 2023, *arXiv e-prints*, p. [arXiv:2309.15948](#)
- Aubert D., Teyssier R., 2010, *ApJ*, **724**, 244
- Bemis A. R., Wilson C. D., 2023, *ApJ*, **945**, 42
- Benincasa S. M., Wadsley J., Couchman H. M. P., Keller B. W., 2016, *MNRAS*, **462**, 3053
- Bertoldi F., McKee C. F., 1992, *ApJ*, **395**, 140
- Bolatto A. D., Leroy A. K., Rosolowsky E., Walter F., Blitz L., 2008, *ApJ*, **686**, 948
- Brinchmann J., Charlot S., White S. D. M., Tremonti C., Kauffmann G., Heckman T., Brinkmann J., 2004, *MNRAS*, **351**, 1151
- Brucy N., Hennebelle P., Colman T., 2024a, *arXiv e-prints*, p. [arXiv:2404.17368](#)
- Brucy N., Hennebelle P., Colman T., Klessen R. S., Le Yhuelic C., 2024b, *arXiv e-prints*, p. [arXiv:2404.17374](#)
- Burkhart B., 2018, *ApJ*, **863**, 118
- Castaing B., 1996, *Journal de Physique II*, **6**, 105
- Chabrier G., 2003, *PASP*, **115**, 763
- Ciesla L., et al., 2023, *A&A*, **672**, A191
- Courty S., Alimi J. M., 2004, *A&A*, **416**, 875
- Daddi E., et al., 2010, *ApJ*, **714**, L118
- Dessauges-Zavadsky M., et al., 2019, *Nature Astronomy*, **3**, 1115
- Dessauges-Zavadsky M., et al., 2023, *MNRAS*, **519**, 6222
- Duncan K., et al., 2019, *ApJ*, **876**, 110
- Eibensteiner C., et al., 2023, *A&A*, **675**, A37
- Ejdetjärn T., Agertz O., Östlin G., Renaud F., Romeo A. B., 2022, *MNRAS*, **514**, 480
- Elmegreen B. G., 1989, *ApJ*, **338**, 178
- Faucher-Giguère C.-A., Quataert E., Hopkins P. F., 2013, *MNRAS*, **433**, 1970
- Federrath C., 2015, *MNRAS*, **450**, 4035
- Federrath C., Klessen R. S., 2012, *ApJ*, **761**, 156
- Federrath C., Klessen R. S., 2013, *ApJ*, **763**, 51
- Federrath C., Roman-Duval J., Klessen R. S., Schmidt W., Mac Low M. M., 2010, *A&A*, **512**, A81
- Feldmann R., Gnedin N. Y., 2011, *ApJ*, **727**, L12
- Feldmann R., et al., 2023, *MNRAS*, **522**, 3831
- Förster Schreiber N. M., Wuyts S., 2020, *ARA&A*, **58**, 661
- Fudamoto Y., et al., 2022, *ApJ*, **934**, 144
- Gallagher M. J., et al., 2018a, *ApJ*, **858**, 90
- Gallagher M. J., et al., 2018b, *ApJ*, **868**, L38
- Girma E., Teyssier R., 2024, *MNRAS*, **527**, 6779
- Grisdale K., Agertz O., Romeo A. B., Renaud F., Read J. I., 2017, *MNRAS*, **466**, 1093
- Grisdale K., Agertz O., Renaud F., Romeo A. B., 2018, *MNRAS*, **479**, 3167
- Grisdale K., Agertz O., Renaud F., Romeo A. B., Devriendt J., Slyz A., 2019, *MNRAS*, **486**, 5482
- Grudić M. Y., Hopkins P. F., Faucher-Giguère C.-A., Quataert E., Murray N., Kereš D., 2018, *MNRAS*, **475**, 3511
- Grudić M. Y., Hopkins P. F., Lee E. J., Murray N., Faucher-Giguère C.-A., Johnson L. C., 2019, *MNRAS*, **488**, 1501
- Haardt F., Madau P., 1996, *ApJ*, **461**, 20
- Hahn O., Abel T., 2011, *MNRAS*, **415**, 2101
- He H., Bottrell C., Wilson C., Moreno J., Burkhart B., Hayward C. C., Hernquist L., Twum A., 2023, *ApJ*, **950**, 56
- Heintz K. E., et al., 2022, *ApJ*, **934**, L27
- Hennebelle P., Chabrier G., 2011, *ApJ*, **743**, L29
- Herrera-Camus R., et al., 2022, *A&A*, **665**, L8
- Heyer M., Krawczyk C., Duval J., Jackson J. M., 2009, *ApJ*, **699**, 1092
- Heyer M., Gutermuth R., Urquhart J. S., Csengeri T., Wienen M., Leurini S., Menten K., Wyrowski F., 2016, *A&A*, **588**, A29
- Hopkins P. F., 2013, *MNRAS*, **430**, 1880
- Hopkins P. F., Quataert E., Murray N., 2011, *MNRAS*, **417**, 950
- Hopkins P. F., Quataert E., Murray N., 2012, *MNRAS*, **421**, 3488
- Hopkins P. F., Narayanan D., Murray N., 2013a, *MNRAS*, **432**, 2647
- Hopkins P. F., Narayanan D., Murray N., Quataert E., 2013b, *MNRAS*, **433**, 69
- Hopkins P. F., Kereš D., Oñorbe J., Faucher-Giguère C.-A., Quataert E., Murray N., Bullock J. S., 2014, *MNRAS*, **445**, 581
- Hopkins P. F., et al., 2018, *MNRAS*, **480**, 800
- Jiménez-Donaire M. J., et al., 2019, *ApJ*, **880**, 127
- Kennicutt Robert C. J., 1998, *ApJ*, **498**, 541
- Kim C.-G., Ostriker E. C., 2015, *ApJ*, **802**, 99
- Kim J.-h., et al., 2014, *ApJS*, **210**, 14
- Kim J.-h., et al., 2016, *ApJ*, **833**, 202
- Klessen R. S., Glover S. C. O., 2016, *Saas-Fee Advanced Course*, **43**, 85
- Krahm G., Finn M. K., Indebetouw R., Johnson K. E., Kamenetzky J., Bemis A., 2024, *ApJ*, **964**, 166
- Kraljic K., Renaud F., Bournaud F., Combes F., Elmegreen B., Emsellem E., Teyssier R., 2014, *ApJ*, **784**, 112
- Kraljic K., et al., 2024, *A&A*, **682**, A50
- Kretschmer M., Teyssier R., 2020, *MNRAS*, **492**, 1385
- Krumholz M. R., McKee C. F., 2005, *ApJ*, **630**, 250
- Krumholz M. R., Dekel A., McKee C. F., 2012, *ApJ*, **745**, 69
- Krumholz M. R., McKee C. F., Bland-Hawthorn J., 2019, *ARA&A*, **57**, 227
- Larson R. B., 1981, *MNRAS*, **194**, 809
- Lee E. J., Miville-Deschênes M.-A., Murray N. W., 2016, *ApJ*, **833**, 229
- Leethochawalit N., et al., 2023, *ApJ*, **942**, L26
- Leitherer C., et al., 1999, *ApJS*, **123**, 3
- Leroy A. K., et al., 2013, *AJ*, **146**, 19
- Leroy A. K., et al., 2015, *ApJ*, **801**, 25
- Leroy A. K., et al., 2016, *ApJ*, **831**, 16
- Leroy A. K., et al., 2017, *ApJ*, **846**, 71
- Li H., Gnedin O. Y., Gnedin N. Y., 2018, *ApJ*, **861**, 107
- Li H., Vogelsberger M., Marinacci F., Sales L. V., Torrey P., 2020, *MNRAS*, **499**, 5862
- Li H., Vogelsberger M., Bryan G. L., Marinacci F., Sales L. V., Torrey P., 2022, *MNRAS*, **514**, 265
- Mac Low M.-M., 1999, *ApJ*, **524**, 169
- Mac Low M.-M., Klessen R. S., Burkert A., Smith M. D., 1998, *Phys. Rev. Lett.*, **80**, 2754
- McKee C. F., Ostriker E. C., 2007, *ARA&A*, **45**, 565
- Miville-Deschênes M.-A., Murray N., Lee E. J., 2017, *ApJ*, **834**, 57
- Müller J., 2000, *Journal of Research of the National Institute of Standards and Technology*, **105**, 551
- Neumann L., et al., 2023, *MNRAS*, **521**, 3348
- Nobels F. S. J., Schaye J., Schaller M., Ploekinger S., Chaikin E., Richings A. J., 2024, *MNRAS*, **532**, 3299
- Núñez-Castiñeyra A., Nezri E., Devriendt J., Teyssier R., 2021, *MNRAS*, **501**, 62
- Ohlin L., Renaud F., Agertz O., 2019, *MNRAS*, **485**, 3887
- Orr M. E., et al., 2018, *MNRAS*, **478**, 3653
- Padoan P., Nordlund Å., 2011, *ApJ*, **730**, 40
- Padoan P., Haugbølle T., Nordlund Å., 2012, *ApJ*, **759**, L27
- Parlanti E., Carniani S., Pallottini A., Cignoni M., Cresci G., Kohandel M., Mannucci F., Marconi A., 2023, *A&A*, **673**, A153
- Petkova M. A., et al., 2023, *MNRAS*, **525**, 962
- Polzin A., Kravtsov A. V., Semenov V. A., Gnedin N. Y., 2024, *arXiv e-prints*, p. [arXiv:2407.11125](#)
- Pope A., et al., 2023, *ApJ*, **951**, L46
- Posses A. C., et al., 2023, *A&A*, **669**, A46
- Querejeta M., et al., 2019, *A&A*, **625**, A19
- Raiteri C. M., Villata M., Navarro J. F., 1996, *A&A*, **315**, 105

- Renaud F., Kraljic K., Bournaud F., 2012, *ApJ*, **760**, L16
- Renaud F., et al., 2013, *MNRAS*, **436**, 1836
- Renaud F., Bournaud F., Kraljic K., Duc P. A., 2014, *MNRAS*, **442**, L33
- Renaud F., Agertz O., Read J. I., Ryde N., Andersson E. P., Bensby T., Rey M. P., Feuillet D. K., 2021a, *MNRAS*, **503**, 5846
- Renaud F., Agertz O., Andersson E. P., Read J. I., Ryde N., Bensby T., Rey M. P., Feuillet D. K., 2021b, *MNRAS*, **503**, 5868
- Renaud F., Segovia Otero Á., Agertz O., 2022, *MNRAS*, **516**, 4922
- Renaud F., Agertz O., Romeo A. B., 2024, *A&A*, **687**, A91
- Rizzo F., et al., 2023, *arXiv e-prints*, p. arXiv:2303.16227
- Roca-Fàbrega S., et al., 2021, *ApJ*, **917**, 64
- Rodighiero G., et al., 2011, *ApJ*, **739**, L40
- Roman-Oliveira F., Fraternali F., Rizzo F., 2023, *MNRAS*, **521**, 1045
- Romeo A. B., Agertz O., Renaud F., 2023, *MNRAS*, **518**, 1002
- Rosen A., Bregman J. N., 1995, *ApJ*, **440**, 634
- Rosolowsky E., Leroy A., 2006, *PASP*, **118**, 590
- Rosolowsky E., et al., 2021, *MNRAS*, **502**, 1218
- Saintonge A., Catinella B., 2022, *ARA&A*, **60**, 319
- Schinnerer E., Leroy A. K., 2024, *arXiv e-prints*, p. arXiv:2403.19843
- Schmidt W., Federrath C., 2011, *A&A*, **528**, A106
- Schmidt W., et al., 2014, *MNRAS*, **440**, 3051
- Scholte D., et al., 2024, *arXiv e-prints*, p. arXiv:2408.03996
- Schruba A., Kruijssen J. M. D., Leroy A. K., 2019, *ApJ*, **883**, 2
- Segovia Otero Á., Renaud F., Agertz O., 2022, *MNRAS*, **516**, 2272
- Semenov V. A., Kravtsov A. V., Gnedin N. Y., 2016, *ApJ*, **826**, 200
- Semenov V. A., Kravtsov A. V., Gnedin N. Y., 2017, *ApJ*, **845**, 133
- Semenov V. A., Kravtsov A. V., Gnedin N. Y., 2018, *ApJ*, **861**, 4
- Solomon P. M., Rivolo A. R., Barrett J., Yahil A., 1987, *ApJ*, **319**, 730
- Speagle J. S., Steinhardt C. L., Capak P. L., Silverman J. D., 2014, *ApJS*, **214**, 15
- Stone J. M., Ostriker E. C., Gammie C. F., 1998, *ApJ*, **508**, L99
- Sun J., et al., 2018, *ApJ*, **860**, 172
- Sun J., et al., 2020a, *ApJ*, **892**, 148
- Sun J., et al., 2020b, *ApJ*, **901**, L8
- Sun J., et al., 2022, *AJ*, **164**, 43
- Sun J., et al., 2023, *ApJ*, **945**, L19
- Sutherland R. S., Dopita M. A., 1993, *ApJS*, **88**, 253
- Tacconi L. J., et al., 2018, *ApJ*, **853**, 179
- Tacconi L. J., Genzel R., Sternberg A., 2020, *ARA&A*, **58**, 157
- Tamburro D., Rix H. W., Leroy A. K., Mac Low M. M., Walter F., Kennicutt R. C., Brinks E., de Blok W. J. G., 2009, *AJ*, **137**, 4424
- Teyssier R., 2002, *A&A*, **385**, 337
- Trebitsch M., Blaizot J., Rosdahl J., Devriendt J., Slyz A., 2017, *MNRAS*, **470**, 224
- Trussler J. A. A., et al., 2023, *MNRAS*, **523**, 3423
- Übler H., et al., 2019, *ApJ*, **880**, 48
- Utomo D., et al., 2018, *ApJ*, **861**, L18
- Wei L. H., Keto E., Ho L. C., 2012, *ApJ*, **750**, 136
- Wetzel A., et al., 2023, *ApJS*, **265**, 44
- Wilson C. D., Bemis A., Ledger B., Klimi O., 2023, *MNRAS*, **521**, 717
- Wise J. H., Turk M. J., Norman M. L., Abel T., 2012, *ApJ*, **745**, 50
- Wisnioski E., et al., 2015, *ApJ*, **799**, 209
- Woosley S. E., Heger A., 2007, *Phys. Rep.*, **442**, 269
- Wu J., Evans Neal J. I., Shirley Y. L., Knez C., 2010, *ApJS*, **188**, 313
- Wuyts S., et al., 2011, *ApJ*, **742**, 96
- Zakardjian A., et al., 2023, *A&A*, **678**, A171

This paper has been typeset from a \LaTeX file prepared by the author.